

satellite. A discontinuity between a core and a mantle is possible but not required by the data. Models with a constant silicate mass fraction throughout the body cannot account for the determined quadrupole coefficients. The data exclude fully differentiated models in which the core would be composed of unhydrated silicates and the mantle would be composed of pure ice. If the mantle contains 10% in mass of silicates, the core extends to 630 km in radius and has a silicate mass fraction of 40%. A continuous model in which the silicates are more concentrated toward the center of the body than in the outer layers is allowed by the gravity data but excluded by thermal evolution considerations. The one model that fits the gravity data and is self-consistent when energy transport and ice melting are qualitatively considered is an almost undifferentiated Rhea, in which a very large uniform core is surrounded by a relatively thin ice shell containing no rock at all.

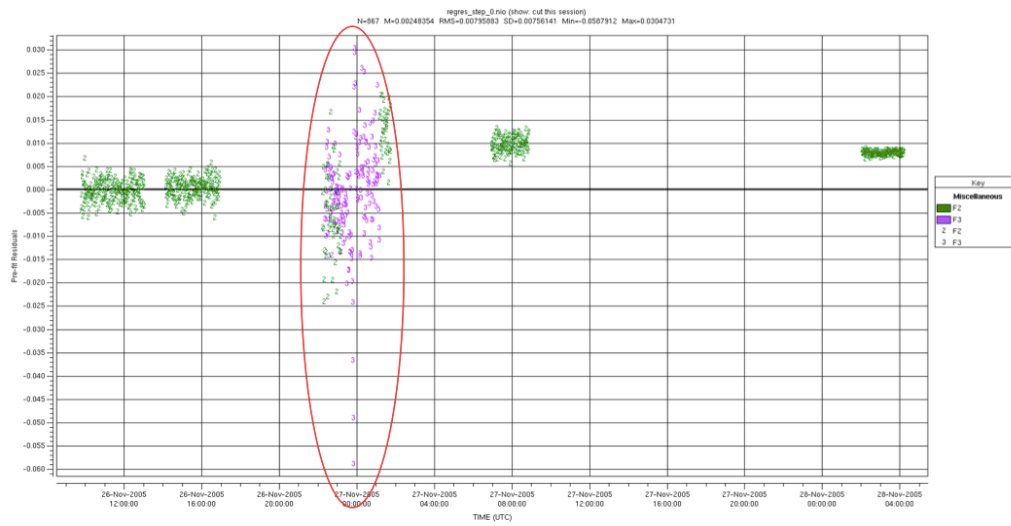


Figure 3-2a: Pre-fit residuals of a Rhea gravity experiment.

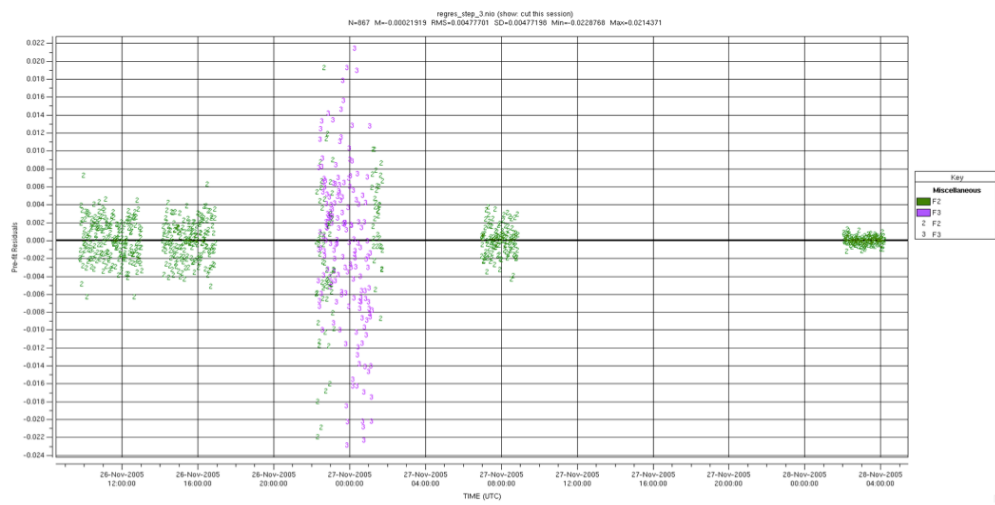


Figure 3-2b: Post-fit residuals of a Rhea gravity experiment.

Figure 3-4 shows that the steering worked very well; the offset of approximately 10 Hz in this case is typically the result of small errors in the prediction ephemerides and will become insignificant once the actual state vectors are calculated (see next sections).

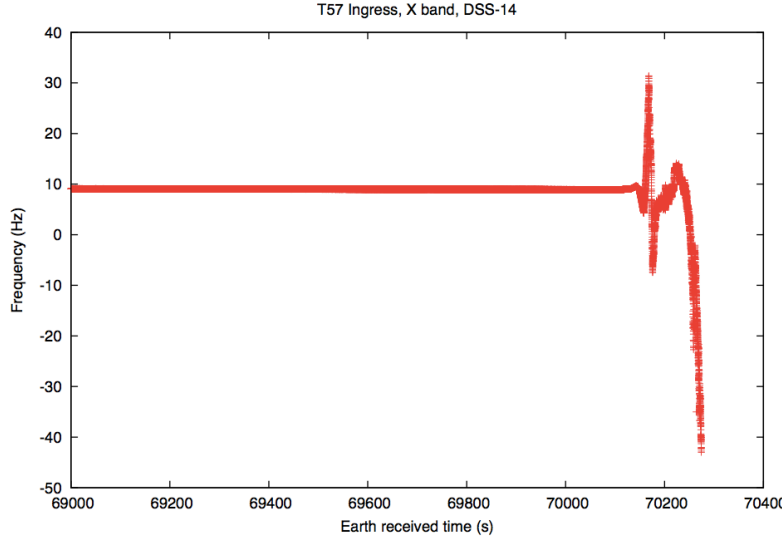


Figure 3-4: Frequency of the Cassini carrier at the output of the X-band RSR during the T57I occultation ingress observation. RSR complex samples (I/Q pairs) were recorded at 16 kHz (file S51TIOI2009173\_1845NNNX14RD.1A2). Data were processed using 512-point FFTs, with running averages over 8 transforms slipped by one transform per calculation (0.032 s per output point, 0.256 s per independent point). Horizontal axis gives time since UT midnight in seconds at the DSS-14 receiving antenna.

### 3.2.1.1.2 Using the Ephemeris

The next step in the processing is to use the highest quality spacecraft and planetary ephemerides to reconstruct the geometry of the occultation and to determine the bending angles that correspond to the frequencies observed on the ground. The ephemeris for the Cassini mission is in the form of SPICE kernels, which can be used with the NAIF toolkit (<ftp://naif.jpl.nasa.gov/pub/naif/toolkit>), a suite of routines users can incorporate into their own analysis software. The SPICE kernels for the Cassini mission (<ftp://naif.jpl.nasa.gov/pub/naif/CASSINI/kernels>) are in binary or text format, and different kernels contain information about various bodies. For example, the SP kernels are binary files containing the position and velocity state vectors for Saturn, its satellites, the Sun, the Earth, and the spacecraft. PC kernels are text files containing the masses and rotational parameters for various bodies. For the analysis of the T57I occultation, we used:

```
KERNELS_TO_LOAD=()
'100209AP_RE_90165_18018.bsp',
'naif0009.tls',
'cpck17Aug2009.tpc',
'090806R_SCPS_09168_09184.bsp',
'Earthstns_itrf93_050714.bsp',
'Earth_031228_231229_predict.bpc')
```

traditionally used the phase). Once the de-trending had been completed, it was possible to carry out the inversion to obtain the atmospheric temperature-pressure profile that is consistent with the observed frequency record.

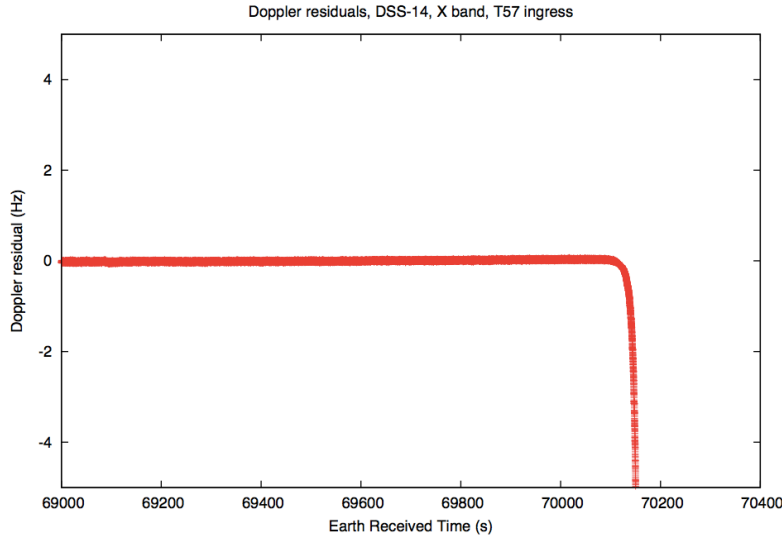


Figure 3-5: Doppler residuals for T57I, DSS-14, X band.

### 3.2.1.1.3 Abel Inversion

The assumption of spherical symmetry imposed upon the atmosphere of Titan greatly simplifies the analysis task. The inversion is then analogous to a central force problem in celestial mechanics. The ‘force’ is the gradient of the index of refraction  $n(r)$ , assumed by spherical symmetry to be a function solely of the radius  $r$ , which tugs on the ray and changes its direction as it traverses the atmosphere. Because the force is central, each successive ray is confined to a plane containing the spacecraft, the center of Titan, and the receiving DSN antenna on Earth. Successive ray paths will be in different planes because the spacecraft and DSN antenna are continually moving; however, planar geometry can be used to obtain the bending angle within each plane. With the assumption of spherical symmetry, it can be shown (Phinney and Anderson, 1968) that there is a unique Abel transform relating the bending angle to the refractivity of the atmosphere. There is an analog of total angular momentum conservation with which we can obtain the minimum radius of the *ray periapsis*  $R$  without ever determining the actual ray trajectory. Indeed, the path of the ray is neither required nor determined using this method.

The Abel integral relates the refractivity and bending angle (defined above) to the impact parameter  $a$ , which is the product of radius  $R$  and index of refraction  $n$  at the ray’s closest approach. The bending angle  $\alpha$  is computed from the geometry and the Earth-received frequency by invoking several conditions. The primary condition, which can be imposed because of the spherical symmetry, is that the ray trajectory remains in a single plane; that plane is defined by the spacecraft, the center of the target, and the receiving DSN antenna. The angle between the spacecraft velocity vector  $v_s$  and the initial ray direction

For example, Kliore *et al.* (2008) show the ionosphere of Titan; see Figure 3-7. The first four sets of radio occultations of the Titan's ionosphere were obtained by the Cassini spacecraft between March 2006 and May 2007. These occultations occurred at middle and high latitudes, at solar zenith angles from about  $86^\circ$  to  $96^\circ$ . The main ionospheric peak was seen, as expected from modeling and previous observations, near 1200 km, with a density of about  $1\text{--}3 \times 10^3 \text{ cm}^{-3}$ . A consistent ledge near 1000 km was also seen, and one of the polar observations found a significant ( $\sim 3 \times 10^3 \text{ cm}^{-3}$ ) layer in the region of 500–600 km. This layer also is seen in other observations with a density varying from about 0.7 to  $1.7 \times 10^3 \text{ cm}^{-3}$ , suggesting a variable production source (or sources) for this peak.

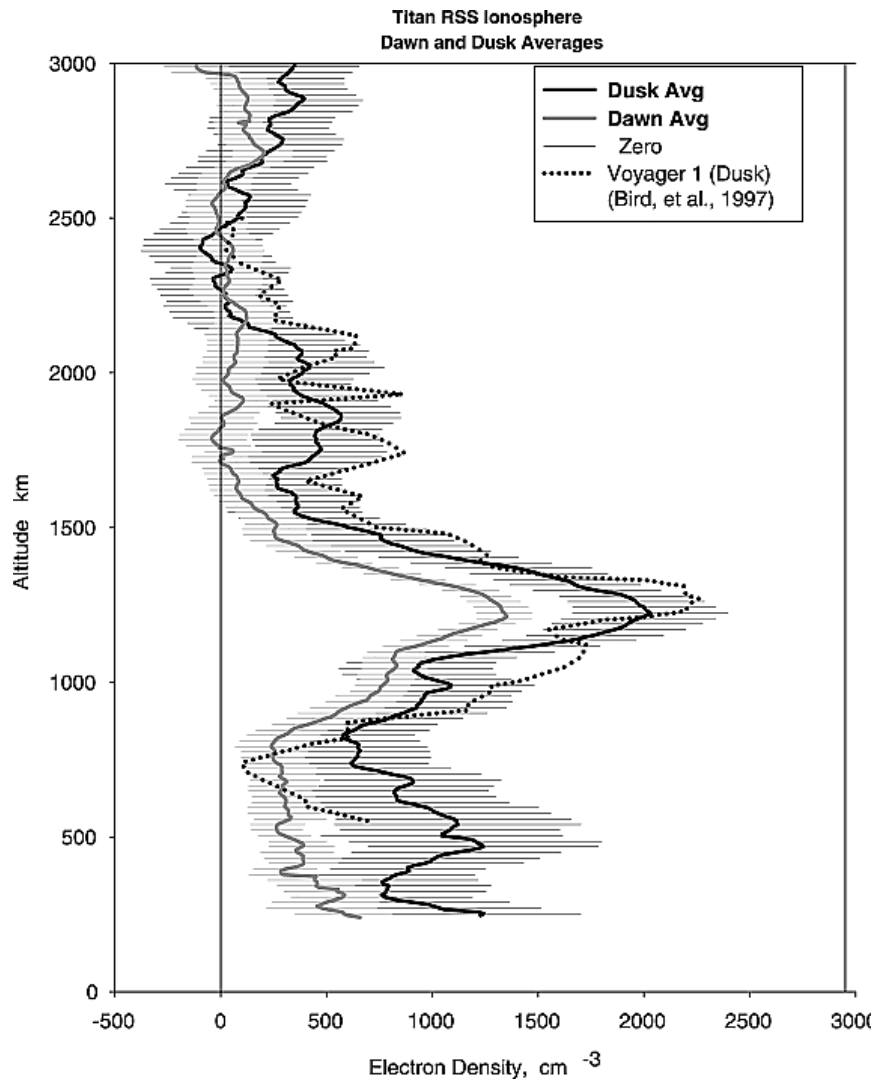


Figure 3-7: From Kliore *et al.*, 2008, observed dawn and dusk and dawn averaged electron density profiles. For T12 and T14 (southern mid latitudes), the dusk observations are also in sunlight, and the dawn observations are in the dark. The Voyager 1 profile is also shown for comparison.

The second component is the near-forward scattered signal, a frequency-broadened signal that originates from incoherent superposition of the signals scattered by ring particles located within the intersection of the main-lobe of the Cassini high-gain antenna and the rings plane (antenna footprint). The Doppler shift caused by the relative motion of the spacecraft, ring particles, and ground station broadens the spectrum of this signal component. The time history of the scattered signal spectra (Figure 3-9) can be used to determine the size distribution of large ( $> 1$  meter) particles as well as other physical properties (Marouf *et al.*, 1983; Zebker *et al.*, 1985).

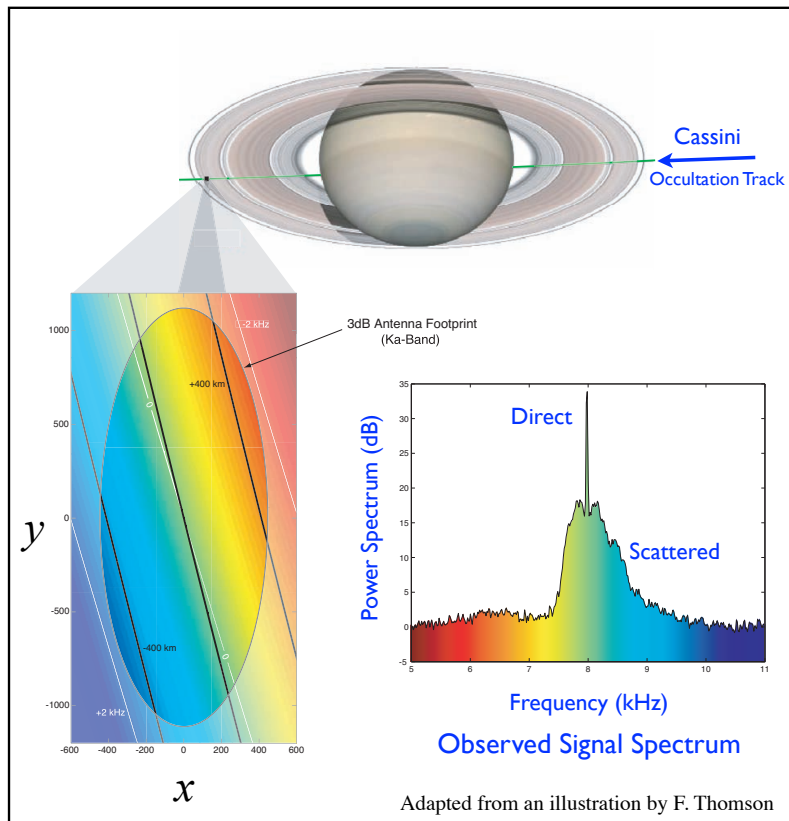


Figure 3-8: Illustration of ring radio occultation direct and scattered signal, and of Doppler mapping over the Ka-band 'footprint' of the Cassini high-gain antenna.

### 3.3.3. RSS Ring Occultations During the Cassini Prime Mission

Twenty-four one-sided radio occultations of Saturn's rings were observed during the Cassini Prime Mission (Table 3-1); additional experiments since the prime mission are listed in Appendix 1 online (see the URL in section 1.0). The spacecraft trajectory is chosen so that the path of the radio signals transmitted from Cassini to an observing ground receiving station would be interrupted by the ring system.

The Prime Mission occultation observations sampled a broad range of ring opening angles,  $B$ . In particular, a set from Revs 7 to 14 of mostly diametric occultations captured

relatively large angles, 19.5-23.5°, allowing detailed profiling of the optically thick Ring B for the first time. Another set from Revs 53-67 of mostly chord occultations sampled small *angles*, 6-10°. The limited intermediate range of angles, 14-15°, was sampled by occultations from Revs 28, 44, and 46. These 24 occultation cuts also sampled a broad range of ring longitudes both inertial and Earth-relative.

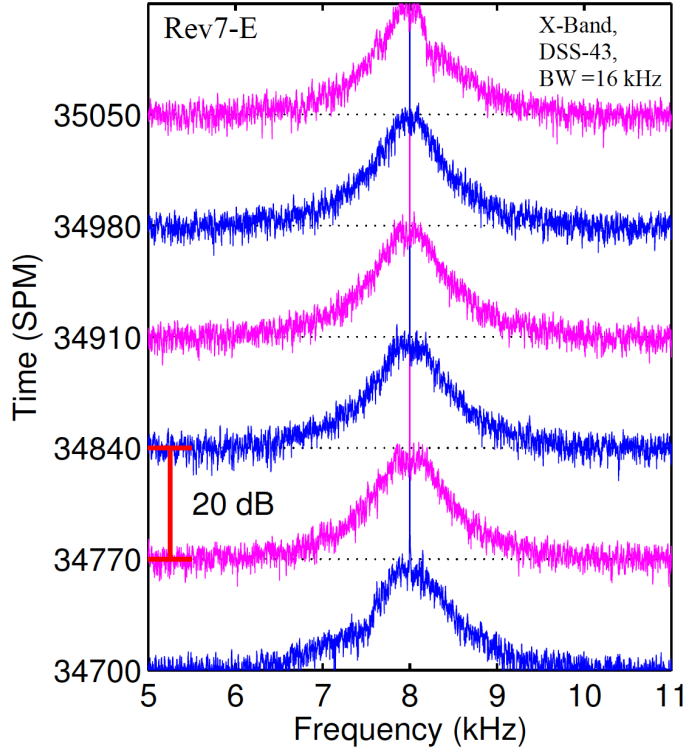


Figure 3-9: Example time sequence of Ring A spectra used to estimate the frequency offset of the direct signal from the center of the recording bandwidth. SPM is seconds past midnight on 2005-05-03.

### 3.3.4. Analysis

Reliably extracting ring structure from the recorded data requires reliable estimation of the variations in phase of the direct sinusoidal signal and amplitudes of the direct and scattered signals as functions of time.

#### 3.3.4.1. Frequency Calibration

Accurate estimation of the signal phase requires compensating the phase from the acquired complex samples for any deterministic offset of the frequency of the direct signal from its expected position at the center of the recording bandwidth. This is accomplished by compensating the phase of the measured I/Q samples as follows:

$$I_c(t) + iQ_c(t) = [I_m(t) + iQ_m(t)] \exp[-i\psi(t)] \quad (17)$$

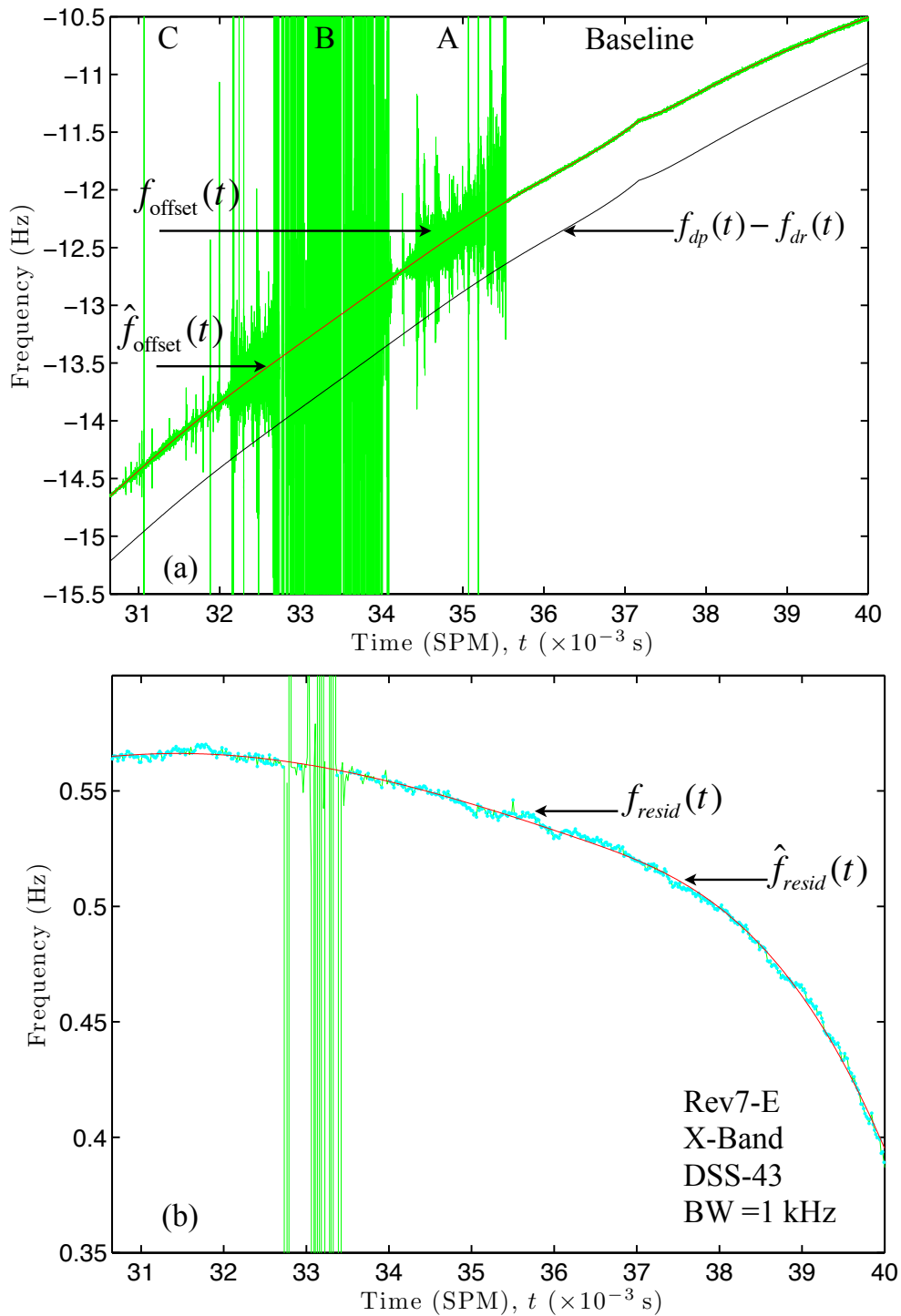


Figure 3-10: Example estimations of direct signal frequency offset (upper) and residual signal frequency (lower). SPM is seconds past midnight 2005-05-03.

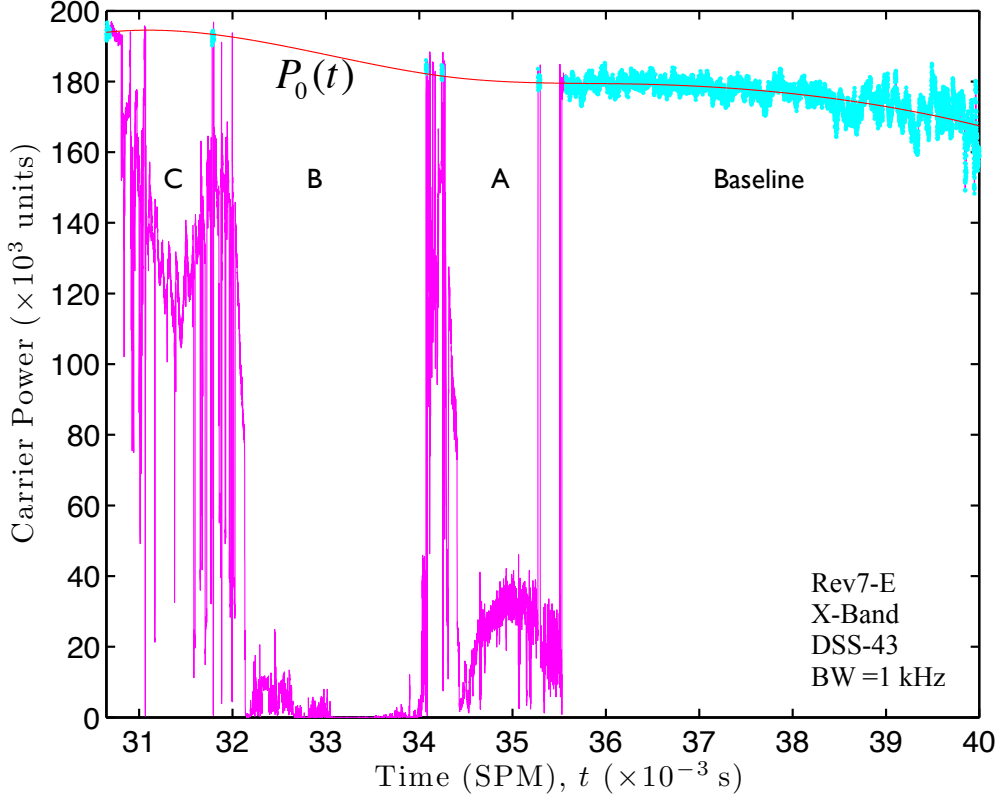


Figure 3-11: Example estimation of free-space signal power  $P_0(t)$ . SPM is seconds past midnight 2005-05-03.

### 3.3.4.3. Radial Interpolation

Complex samples of the calibrated data are uniformly spaced in time. To translate the measurements to ring profiles, the reconstructed spacecraft trajectory is used to calculate the ring intercept radius as a function of time. The calculations are completed using a quasi-inertial Sun-centered reference frame with the light-time included. The procedures were developed for analysis of the Voyager ring occultation experiment and are documented in Rosen (1989). Ring radius accuracy better than few hundred meters is achievable in principle; the primary source of error is the orientation of Saturn's pole. The calculations here are based on the pole orientation in the planetary constants (PCK) files produced by the Cassini Navigation Team (see Table 3-2). The collective set of RSS (and other) occultations may, in turn, be used to improve future estimates of pole orientation and precession rate.

The velocity of the ring-plane intercept point varies radial. As a result, data sampled uniformly in time translate into samples that are non-uniformly spaced in ring radius. Any of several standard numerical interpolation algorithms may be used to interpolate the calibrated data onto a uniform radius grid. Care must be exercised, however, to ensure that interpolation errors are minimized. Below we use the notation

$$\hat{T}(\rho_0) = \hat{T}_R(\rho_0) + i\hat{T}_I(\rho_0) \quad (21)$$

$$\tau_{TH} \cong -\mu_0 \ln[1.205 P_N] \quad (26)$$

where  $P_N$  is the average power of the additive noise in watts. An estimate  $\hat{P}_N$  can be calculated from,

$$\hat{P}_N = \frac{1}{SNR_0} \frac{\dot{\rho}_0}{\Delta R} \quad (27)$$

where  $\Delta R$  is either  $\Delta\rho_0$ , the sample spacing of the diffraction-limited data, or  $\Delta R_{eff}$ , the effective resolution of the reconstructed profiles;  $\dot{\rho}_0$  is the ring plane radial velocity of the ring intercept point; and  $SNR_0$  is the free-space SNR in 1 second integration time, or 1 Hz bandwidth. The latter can be estimated from the recorded I/Q samples. Alternatively, typical X-band values of about 54 and 48 dB-Hz for data collected at the 70- and 34-m ground stations, respectively, may be used.

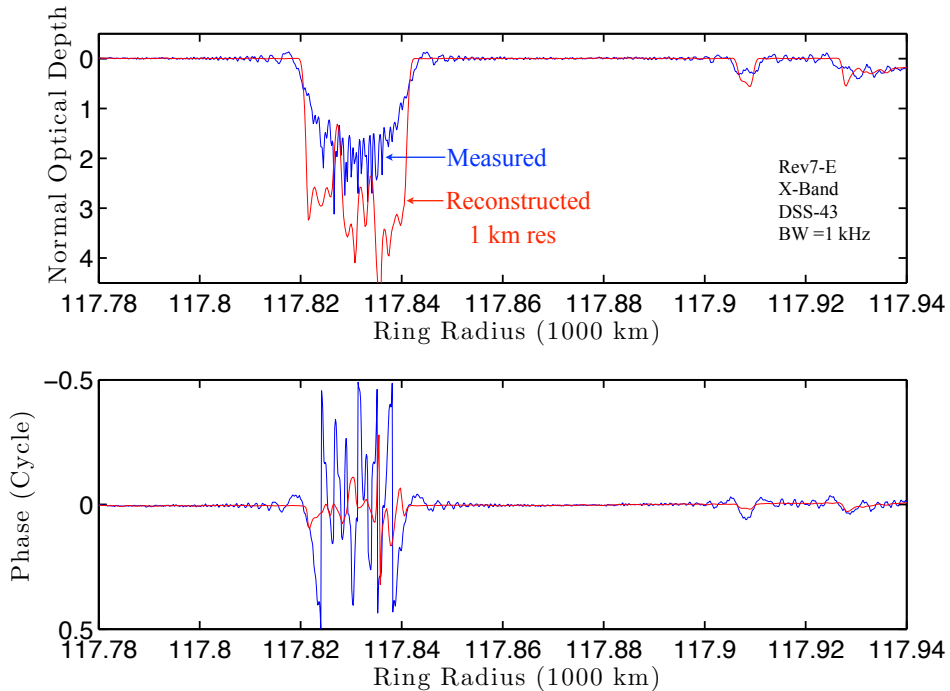


Figure 3-12: Optical depth and phase profile reconstructions from diffraction-limited Rev7-E ring occultation observations of 2005-05-03. The Huygens and ‘Charming’ Ringlets are at radii  $117,830 \pm 11$  km and  $117,908 \pm 3$  km, respectively. The outer edge of the Huygens Gap is at 117,927 km.

Figure 3-13 illustrates the tradeoff discussed above (again, Rev7-E,  $B = -23.5^\circ$ , and  $\dot{\rho}_0 \sim 10$  km/s; see Tables 3-1 and 3-2). The plots show the attenuation of the Titan Ringlet located within the Colombo Gap in inner Ring C at three progressively coarser resolutions of 100 m, 1 km, and 10 km. Also shown are the corresponding  $\tau_{TH}$  levels - horizontal lines of the same color as the corresponding profile. The  $\tau_{TH}$  levels

progressively increase from  $\sim 3.1$  to  $4.0$  to  $5.0$  as the resolution  $\Delta R_{\text{eff}}$  changes from  $100$  m, to  $1$  km, to  $10$  km, respectively.

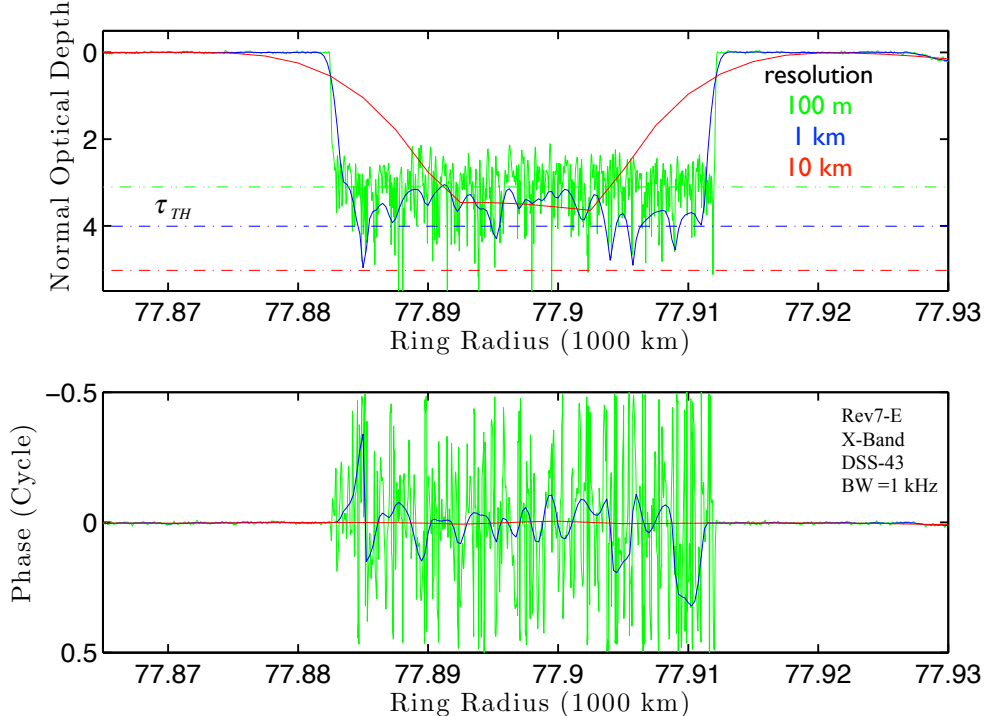


Figure 3-13: Example tradeoff between reconstruction resolution and measurement reliability for the Titan ringlet. The horizontal stippled lines identify the threshold optical depth (SNR  $\sim 1$ ) for each indicated resolution.

At  $100$  m resolution (green profiles in Figure 3-13), almost all structure within the ringlet is obscured by noise; hence, the reconstruction is effectively noise limited and the phase profile is essentially random. The ringlet edge location is recovered with high accuracy, however. The absence of any profile overshoot in the vicinity of transition to a zero value free-space optical depth indicates reliable reconstruction of the diffraction effects.

At fine resolution, diffraction-limited data over a relatively large radial interval  $W$  is required to compute the inverse Fresnel transform. Any inaccuracies exceeding a small fraction of a cycle in the computed phase of the kernel of the inverse transform can cause undesirable artifacts in the reconstructed profiles.

At the  $1$  km resolution (blue profiles), more reliable profiling of ringlet structure is possible only over the fraction of its width where the recovered optical depth exceeds the corresponding threshold level (the horizontal blue line). The phase profile is also well behaved when  $\tau < \tau_{\text{TH}}$ . The edges remain relatively sharp at this resolution. At the coarsest  $10$  km resolution (red profiles), reliable measurement of an ‘average’ optical depth of the ringlet is achieved but the fine structure is lost — for example, the edges are highly smoothed. Relatively large threshold optical depths, such as the  $\tau_{\text{TH}} \sim 5.0$  here, are needed for profiling optically thick ring regions such as parts of Ring B.

The Cassini RSS team carried out a number of bistatic experiments near the Brewster angle at Titan to determine reflectivity and dielectric constant estimates at its three radio wavelengths (Table 3-3).

<b>Table 3-3</b> <b>Cassini Bistatic Radar Experiments</b>		
<b>Start Date</b>	<b>Data Set</b>	<b>Target</b>
2006-03-18	CO-SSA-RSS-1-TBOC1-V1.0	Titan
2006-05-20	CO-SSA-RSS-1-TBOC2-V1.0	Titan
2007-03-25	CO-SSA-RSS-1-TBOC3-V1.0	Titan
2007-07-18	CO-SSA-RSS-1-TBIS1-V1.0	Titan
2008-11-03	CO-SSA-RSS-1-TBOC4-V1.0	Titan
2009-03-27	CO-SSA-RSS-1-TBIS2-V1.0	Titan
2009-04-04	CO-SSA-RSS-1-TBOC5-V1.0	Titan

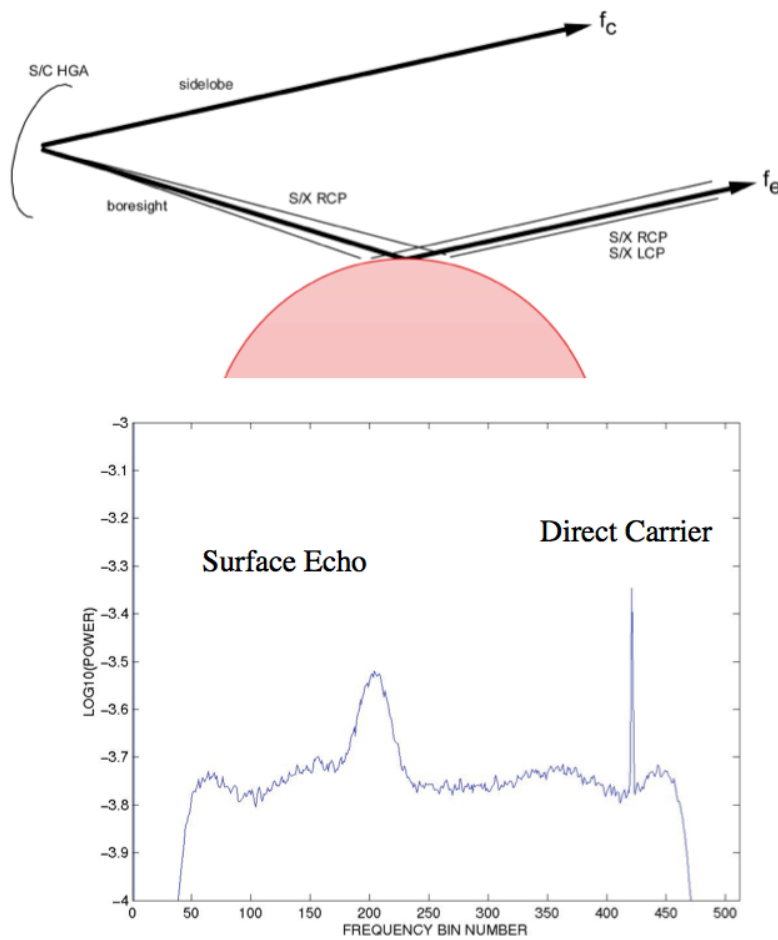


Figure 3-14: Representation of a bistatic radar experiment and resulting spectrum. The directly propagating signal is at frequency bin  $\sim 420$ ; the surface echo extends over bins  $\sim 175$ - $230$ .

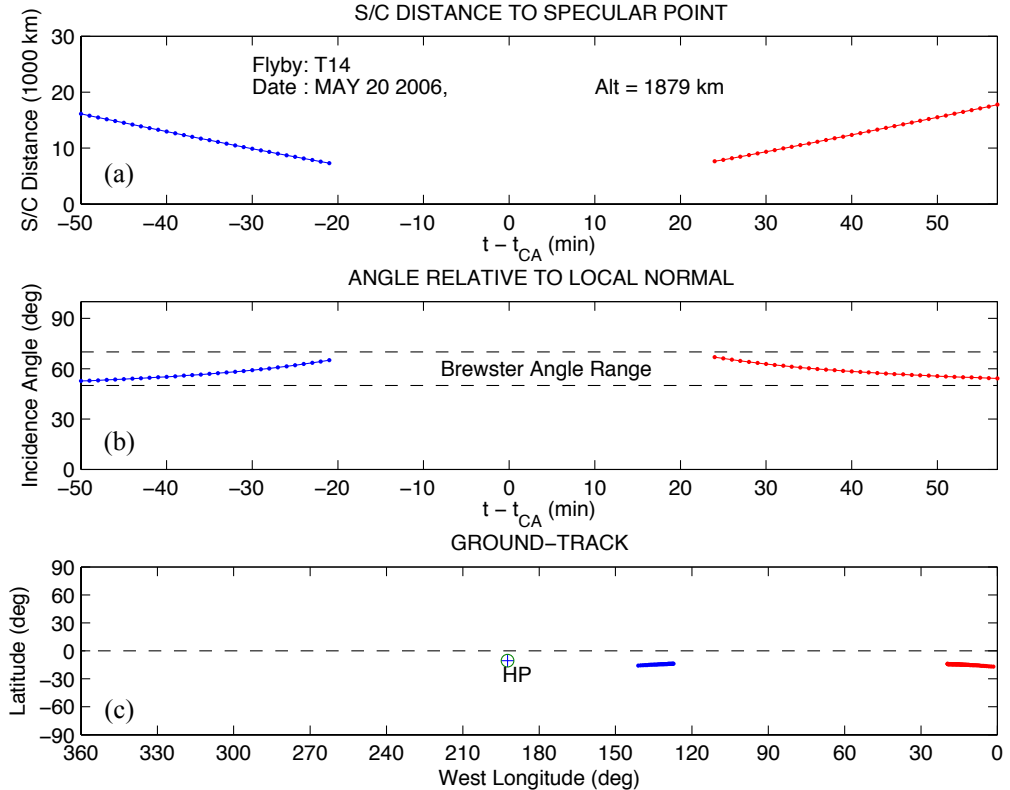


Figure 3-14: Panels (a) and (b) depict selected geometry parameters of the Cassini T14 observations and panel (c) depicts the corresponding ground tracks. The Huygens Probe landing site is shown for reference purposes.

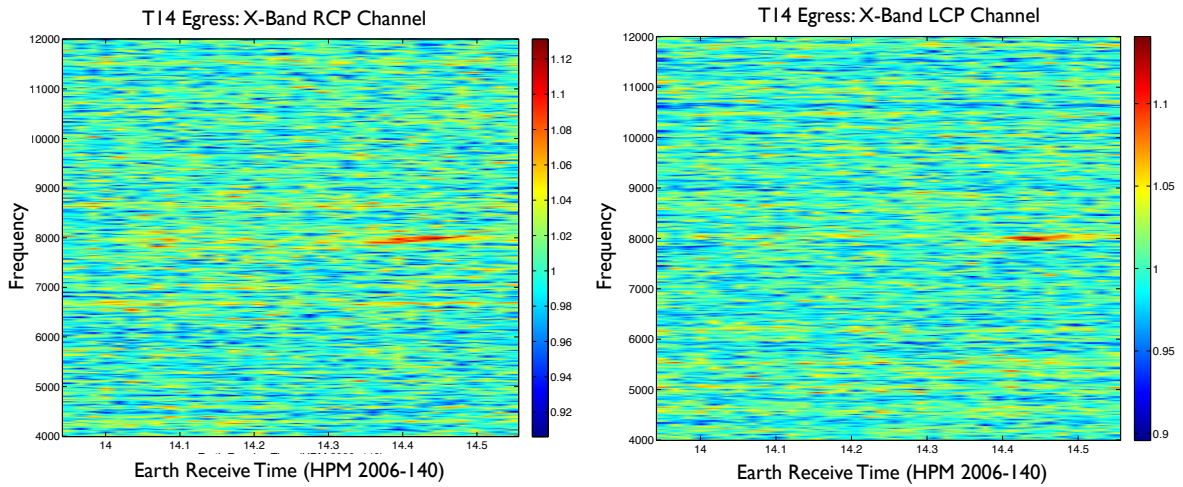
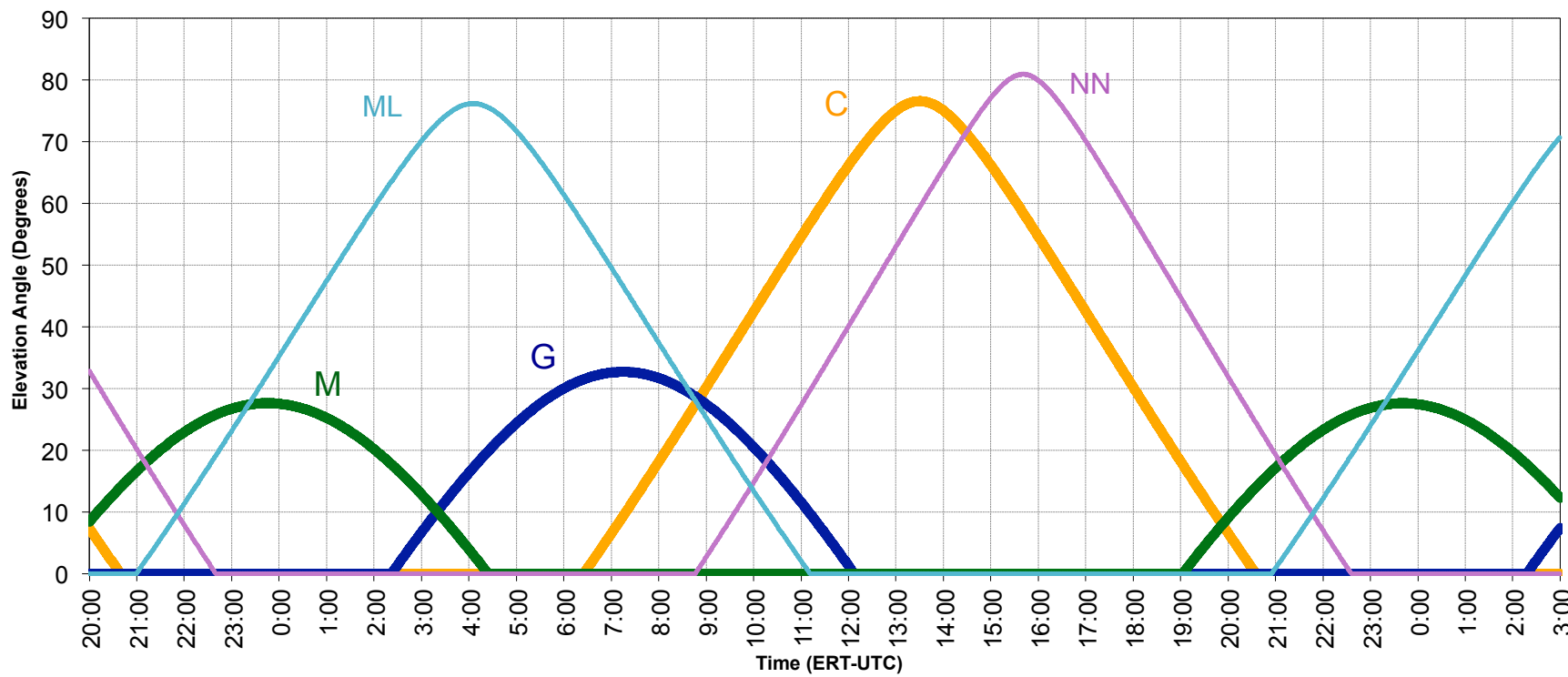
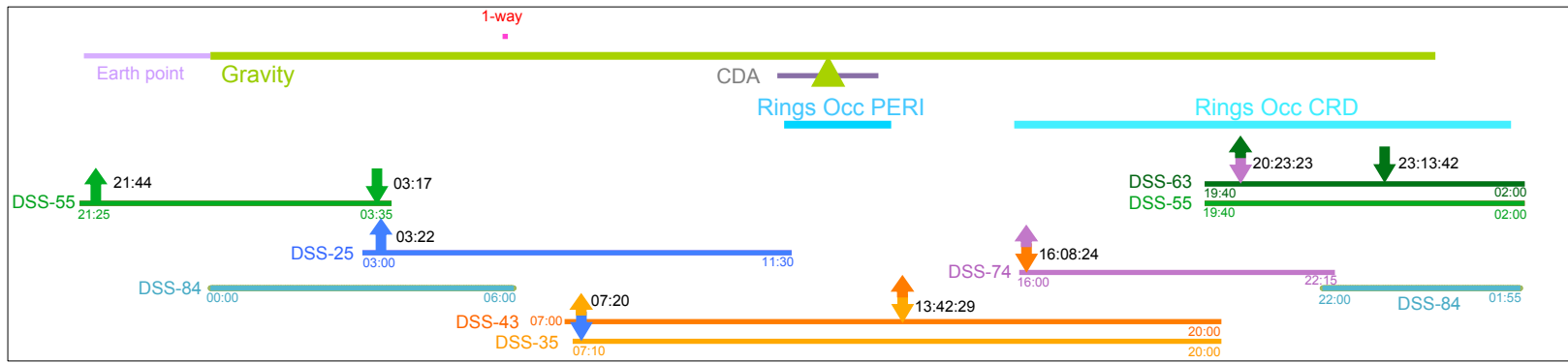


Figure 3-15: Uncalibrated spectrograms of the first positive detection of bistatic echoes from Titan surface observed on the T14 flyby on May 20, 2006 (DOY 140). The weak echoes were simultaneously detectable in both the RCP and LCP 16 kHz bandwidth X-band channels of the 70-m ground station of the Madrid, Spain, DSN complex (DSS-63).

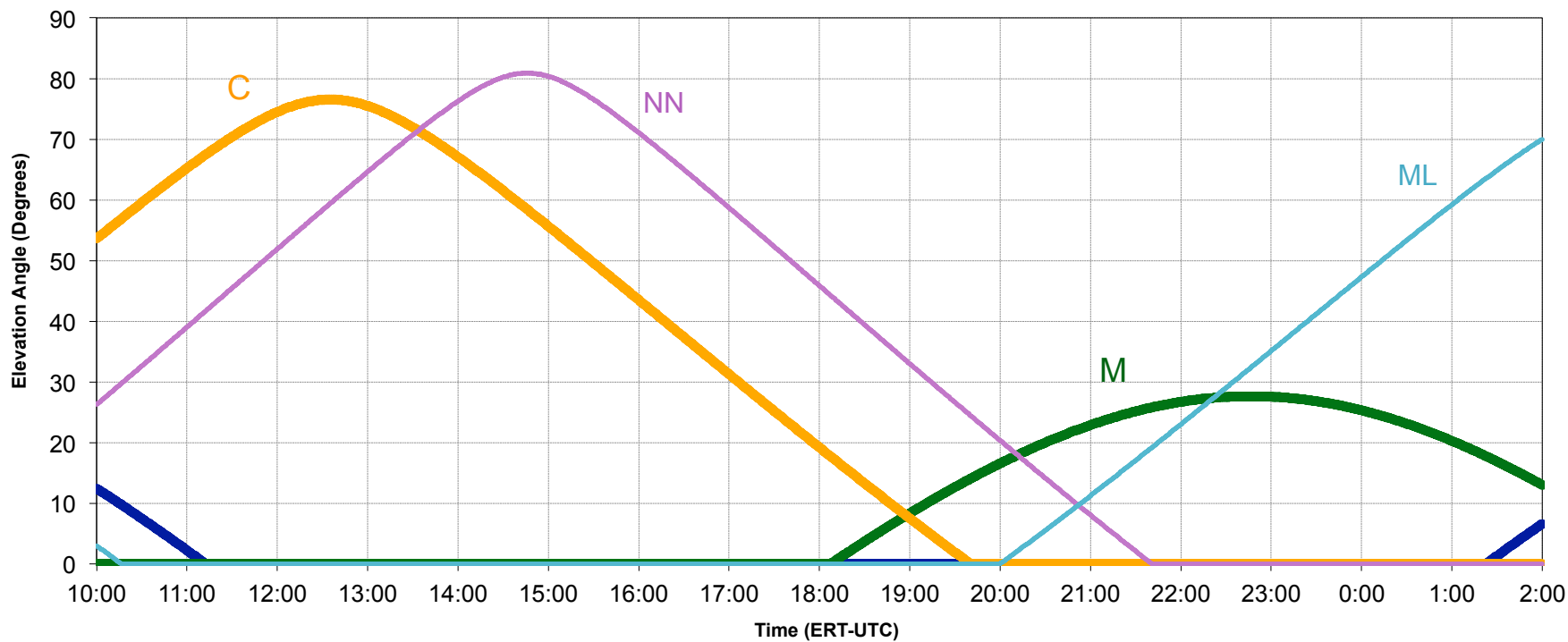
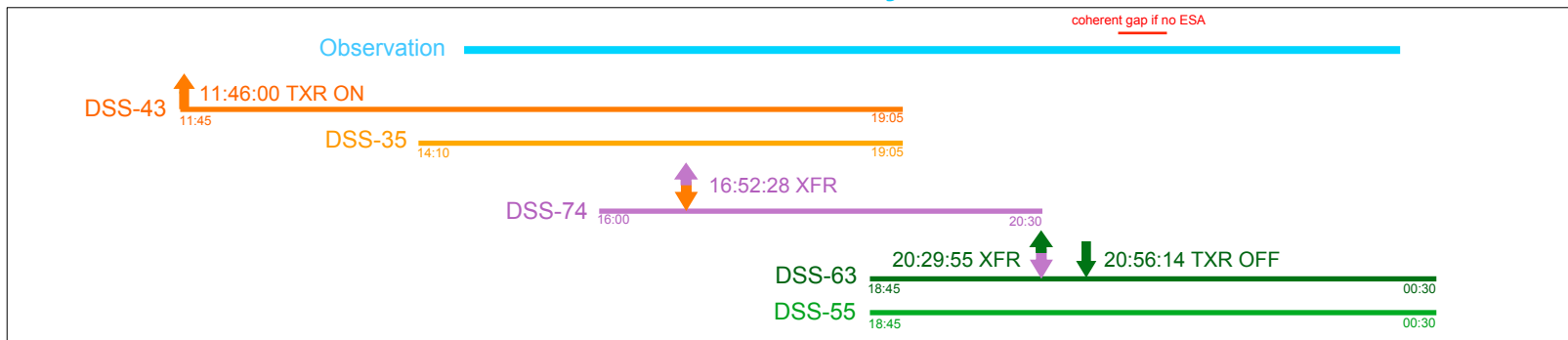
OWLT ~1:15  
RTLT ~ 2:30

## S100 Rev 280 Saturn Gravity Observation & Rings Occultations 2017 173-175 / June 22-24, 2017



OWLT ~1:16  
RTLT ~2:32

## S100 Rev 282 Saturn Rings Occultation 2017 187-188 / July 6-7, 2017



each antenna. A more detailed specification of the key characteristics of the DSN antennas can be found in the DSN Telecommunications Link Design Handbook<sup>1</sup>

## Deep Space Network Resources

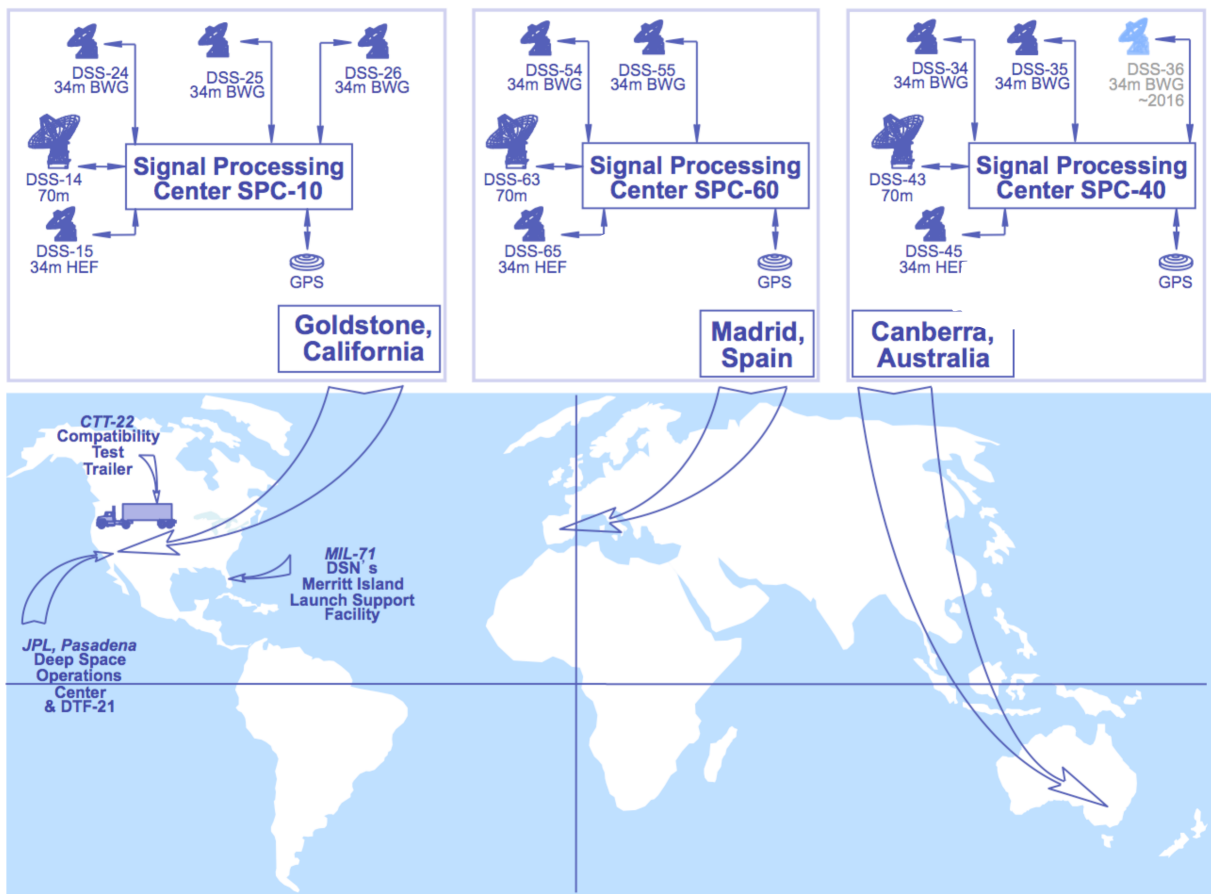


**Figure 2-3. DSN Asset Types and Locations**

<sup>1</sup> DSN Telecommunications Link Design Handbook, Document No. 810-005, Rev. E, Jet Propulsion Laboratory, Pasadena, California